

Micrometer-scale ballistic transport of electron pairs in LaAlO₃/SrTiO₃ nanowires

Michelle Tomczyk,^{1,2} Guanglei Cheng,^{1,2} Hyungwoo Lee,³ Shicheng Lu,^{1,2} Anil Annadi,^{1,2} Joshua P. Veazey,^{1,*} Mengchen Huang,^{1,2} Patrick Irvin,^{1,2} Sangwoo Ryu,³ Chang-Beom Eom,³ and Jeremy Levy^{1,2,†}

¹*Department of Physics and Astronomy, University of Pittsburgh, Pittsburgh, PA 15260, USA*

²*Pittsburgh Quantum Institute, Pittsburgh, PA, 15260 USA*

³*Department of Materials Science and Engineering,
University of Wisconsin-Madison, Madison, WI 53706, USA*

(Dated: November 8, 2021)

High-mobility complex-oxide heterostructures and nanostructures offer new opportunities for extending the paradigm of quantum transport beyond the realm of traditional III-V or carbon-based materials. Recent quantum transport investigations with LaAlO₃/SrTiO₃-based quantum dots have revealed the existence of a strongly correlated phase in which electrons form spin-singlet pairs without becoming superconducting. Here we report evidence for micrometer-scale ballistic transport of electron pairs in quasi-one-dimensional (quasi-1D) LaAlO₃/SrTiO₃ nanowire cavities. In the paired phase, Fabry-Perot-like quantum interference is observed, in sync with conductance oscillations observed in the superconducting regime (at zero magnetic field). Above a critical magnetic field B_p , electron pairs unbind and conductance oscillations shift with magnetic field. These experimental observations extend the regime of ballistic electronic transport to strongly correlated phases.

SrTiO₃-based heterostructures [1] and nanostructures [2] host a wide range of physical phenomena, including magnetism [3] and superconductivity [4]. In particular, LaAlO₃/SrTiO₃ (LAO/STO) heterostructures exhibit strong, tunable spin-orbit coupling [5, 6], a cascade of structural transitions [7], and non-trivial interactions between ferroelastic domain boundaries [8, 9]. LAO/STO-based nanowires possess further surprising behaviors, including *intrinsic* quasi-1D superconductivity [10], and strong electron pairing outside of the superconducting regime [11]. Compared with the 2D superconductor-insulator transition, the nature of correlated electron transport in clean 1D systems remains largely unexplored.

Unlike ballistic semiconducting counterparts, STO-based heterostructures exhibit a relatively short phase coherence, of order ~ 100 nm [12, 13]. However, there is growing evidence that within quasi-1D LAO/STO-based channels, scattering lengths, both elastic and inelastic, may be drastically enhanced. Transport measurements of ~ 10 nm-wide channels at the LAO/STO interface show a nearly two-order-of-magnitude enhancement of Hall mobility, which extends to room temperature [2]. Quasi-1D LAO/STO nanowires exhibit conductance values that hover near the single-channel conductance quantum e^2/h , independent of channel length [14]. There have been stronger claims that the appearance of conductance steps in edge-defined LAO/STO quantum wires implies ballistic transport [15]. However, conductance steps can arise from any point-like constriction [16], and do not imply long-range coherent or ballistic transport. Such conductance steps have also been reported in top-gated STO structures that do not possess a 1D geometry [17].

Quantum interference experiments can provide useful information about electron scattering. Analogous to photonic interference in an optical Fabry-Perot cav-

ity, multiple reflections of electrons from the endpoints of a nanowire cavity can lead to strong interference effects when the elastic scattering length exceeds the cavity length. This interference requires not only phase coherence but also absence of scattering [18]; many systems with long coherence lengths have much shorter elastic scattering lengths. In ballistic Fabry-Perot cavities, the conductance through the cavity oscillates as a function of the Fermi wavelength, which varies with the chemical potential and is usually controlled by a nearby gate electrode. Only a few material systems have been shown to be capable of supporting micrometer-scale quantum interference: suspended single-wall carbon nanotubes [19], high-mobility graphene structures [20], and stacking-fault-free III-V nanowires grown by vapor-liquid-solid techniques [18]. However, these systems often operate in a regime where electron correlations can be neglected; exceptions include Wigner crystal phases, and magnetically and structurally confined one-dimensional systems (i.e., Tomonaga-Luttinger liquids [21]).

In this Letter, we observe evidence of long-range ballistic transport of electron pairs in a complex oxide system. This constitutes a new regime in which strong electronic correlations combine with ballistic electron transport, which is the basis for a remarkable variety of quantum transport phenomena [22], to achieve greater functionality.

To investigate the ballistic nature of transport in LAO/STO nanostructures, quasi-1D Fabry-Perot cavities are created at the LAO/STO interface using conductive atomic force microscope (c-AFM) lithography [23]. A c-AFM tip is placed in contact with and moved across the LAO surface. Positive voltages applied to the tip locally switch the LAO/STO interface to a conductive state (write), while negative voltages applied to the tip locally restore the LAO/STO interface to an insulating

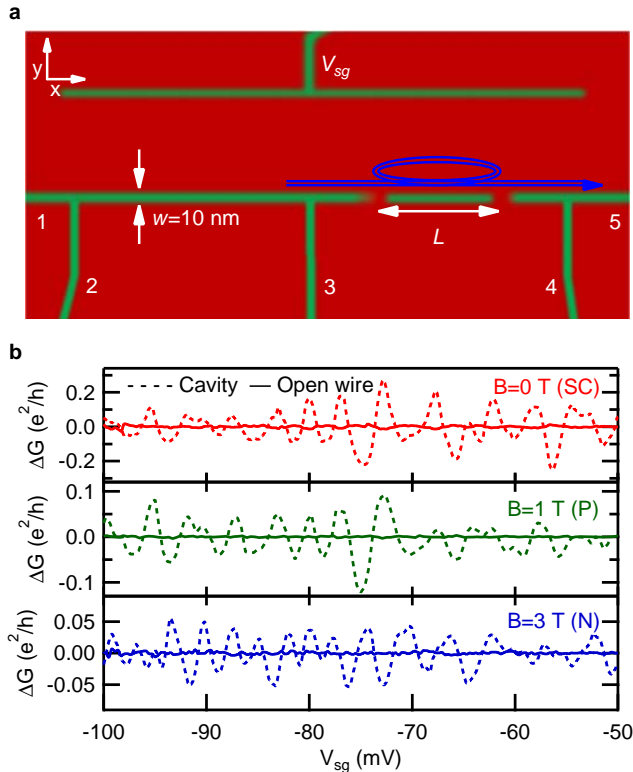


FIG. 1. Device schematic and Fabry-Perot oscillations. (a) Schematic of cavity device defined by two barriers separated by length L . Interference due to coherent scattering in the cavity results in conductance oscillations periodic in Fermi momentum. (b) Background-subtracted zero-bias differential conductance (dI/dV) of the cavity [between voltage leads 3 and 4 in (a)] and the open wire (between leads 2 and 3) in the superconducting (red), paired (green), and normal (blue) phases of Device A clearly reveals large oscillations are only present in the cavity.

state (erase). To create the geometry shown in Fig. 1(a), first a nanowire of width $w \approx 10$ nm is written, followed by erasure steps to create semitransparent barriers at both ends of the cavity. Devices are transferred to a dilution refrigerator within 5 minutes of writing to minimize decay, and are cooled to a base temperature $T = 50$ mK for transport measurements. Current flows through the main channel containing the two barriers. An applied side gate voltage V_{sg} tunes both the transparency of the barriers and the Fermi level in the cavity. Independent voltage leads enable four-terminal measurements of the cavity conductance, as well as that of an adjoining open nanowire, i.e., without barriers. The differential conductance is extracted numerically from $I - V$ curves measured as a function of V_{sg} and magnetic field. Lock-in measurements are performed at reference frequency $f = 13.46$ Hz and amplitude $100 \mu\text{V}$. Cavities of length $L = 0.25 - 4 \mu\text{m}$ were studied, and all show qualitatively similar behavior. Additional details of sample growth

and fabrication of the nanowire and barriers are described elsewhere (see Supplemental Material [24]).

There are three distinct transport regimes [11] as a function of the applied magnetic field: superconducting (SC), paired (P), and normal (N). At temperatures below $T_c \approx 300$ mK, and for out-of-plane magnetic fields below $B_c = \mu_0 H_{c2} \approx 0.2$ T, the LAO/STO interface exhibits a sharp increase in conductance that is attributed to superconductivity, both for 2D heterostructures [4] and 1D nanowires [10]. The regime $B_c < B < B_p$ has been previously identified as a strongly correlated phase in which electrons exist as spin-singlet pairs without forming a superconducting condensate [11]. At sufficiently large magnetic fields (above $B_p \approx 2 - 5$ T), electrons are unpaired and behave normally.

As a function of V_{sg} , typical differential conductance $G = dI/dV$ measurements of the cavity exhibit quasi-periodic oscillations at zero-bias, i.e., $V_{4T} = 0$ V. The variation in conductance G after subtraction of a slowly-varying background (see Supplemental Materials [24] for details) shows clear oscillations in the cavity, but not in the open wire, in all three phases [Fig. 1(b)]. In the superconducting state, the conductance oscillations correspond to modulation of the critical current [24].

The transconductance dG/dV_{sg} (Fig. 2, left), which is computed by numerically differentiating the zero-bias conductance G with respect to side gate, reveals distinct features in the superconducting, paired and normal regimes. The superconducting state is characterized by a sharp conductance peak below $B < B_c$, (Fig. 2, right, shaded red); correspondingly, the transconductance exhibits large oscillations. For $B > B_c$, the oscillations decrease in amplitude, yet remain in phase with the superconducting state modulation, confirming that transport continues to be dominated by electron pair states despite the loss of superconducting coherence. The phase of the oscillations is preserved over the magnetic field range $B_c < B < B_p$ (shaded green), indicating an overall insensitivity to magnetic fields, consistent with the spin-singlet nature of the paired state. For $B > B_p$ (shaded blue), the electron pairs break and the transconductance oscillations shift markedly with magnetic field.

The observed transconductance oscillations are consistent with Fabry-Perot interference in cavity devices up to $4 \mu\text{m}$ in length (Fig. 3). Transmission resonances through the cavity occur when the quantum phase associated with round-trip passage is altered by a change in chemical potential or magnetic (Zeeman) interaction. In the equilibrium case [Fig. 3(a),(c),(e)], in which there is no net bias across the cavity, oscillations appear as a function of the applied side gate voltage, which changes the wavelength of the propagating electron states. In the non-equilibrium regime [Fig. 3(b),(d),(f)], an applied source-drain bias can also change the phase; the result is a characteristic checkerboard pattern similar to what has been reported for other systems such as carbon nan-

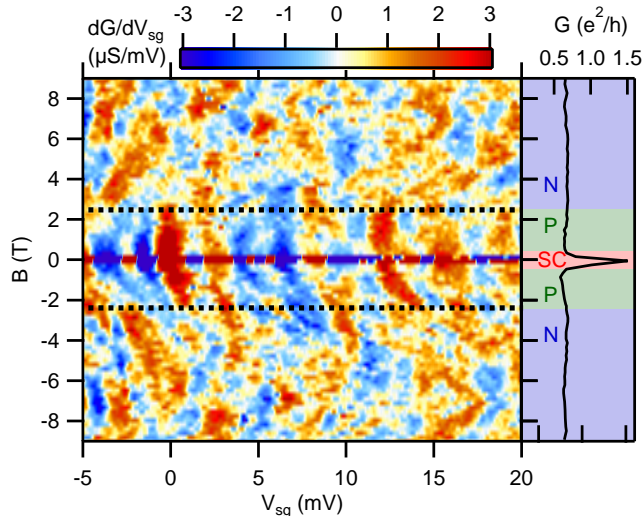


FIG. 2. Magnetic field dependence of conductance oscillations. Left, Transconductance dG/dV_{sg} from a lock-in amplifier measurement of G at small ($100 \mu\text{V}$) bias versus B and V_{sg} for Device B. Alternating red and blue regions correspond to conductance oscillations. Right, A linecut of G versus B at $V_{sg} = 0 \text{ mV}$ shows a sharp peak attributed to superconductivity at $|B| < B_c \approx 0.2 \text{ T}$ (shaded red), while the conductance in the paired (shaded green) and normal (shaded blue) phases is reduced.

otubes [18, 19]. Non-equilibrium effects such as heating and intermode scattering can dephase transport and damp the oscillations at sufficiently high source-drain bias values.

The observation of Fabry-Perot interference in the paired regime provides evidence for ballistic transport of electron pairs in the quasi-1D LAO/STO nanowire system. This result is in sharp contrast to Cooper pair insulators, in which electron pairs surviving outside of the superconducting state are localized [37]. Metallic Bose phases have been observed in both optical lattice [38] and solid state [37] systems, but even in clean superconductors where the mean free path is longer than the superconducting coherence length, the mean free path is only on the order of 10 nm [39]. Additionally, these metallic Bose phases always appear below the upper critical field for superconductivity in the systems. The results observed here in LAO/STO nanowires are distinct due to both the ballistic nature of transport of the uncondensed electron pairs, and the persistence of this ballistic pair state well above the upper critical field for superconductivity in LAO/STO.

While conductance oscillations through the cavity are evident for all values of magnetic field explored (up to 9 T), the open wire shows strong suppression of oscillations in all three phases (Fig. 1 (b)). The root-mean-square amplitude of conductance fluctuations of the open

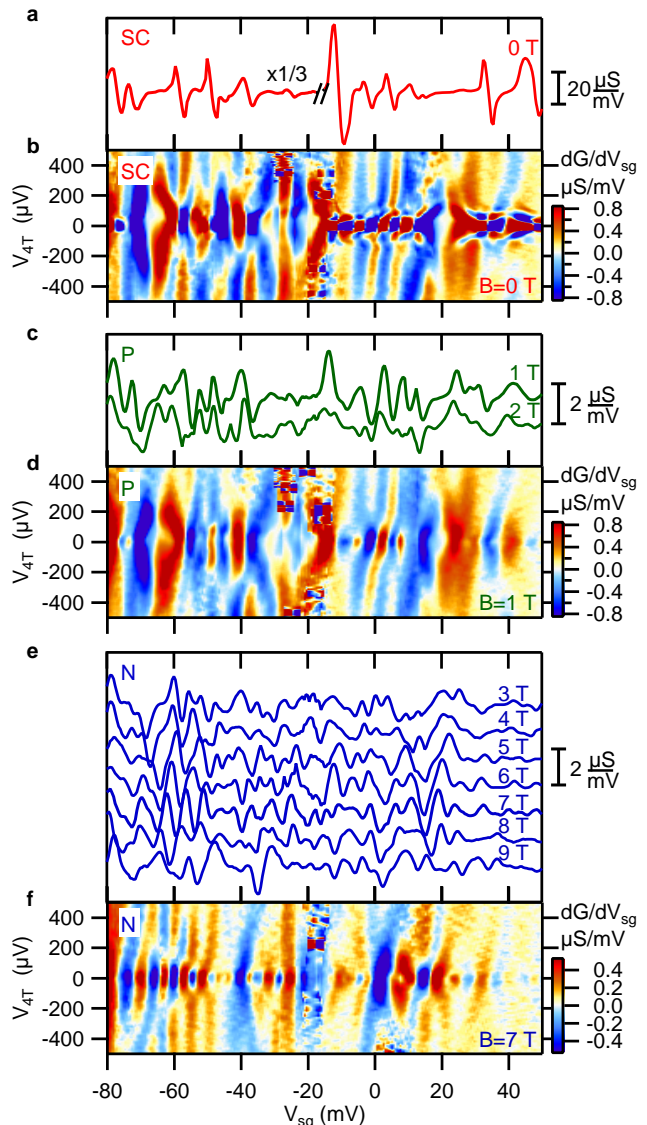


FIG. 3. Fabry-Perot interference signatures at finite bias for an $L = 4 \mu\text{m}$ cavity. (a), (c), (e), Zero-bias dG/dV_{sg} of Device C as a function of V_{sg} at magnetic fields from 0 T (red) to 9 T (blue) in 1 T steps (each curve offset for clarity). The left half of the red curve at $B = 0 \text{ T}$ has been amplified by a factor of 3 compared to the right half. (b), (d), (f), dG/dV_{sg} vs V_{4T} and V_{sg} in the superconducting phase ((b), $B = 0 \text{ T}$), paired phase ((d), $B = 1 \text{ T}$) and normal, unpaired electron phase ((f), $B = 7 \text{ T}$), corresponding to the respective zero-bias linecuts.

wire is reduced by an order of magnitude compared with the cavity, suggesting that imperfections in the nanowires contribute negligibly to scattering. The pattern of behavior described here, for both cavities and open wires, is consistently observed for all of the 50 cavity devices studied.

Devices with a single manufactured barrier, in which no interference is expected to occur, were also studied,

and typical behavior is shown in Supplementary Fig. S7 [24]. Above a conductance value of $\sim e^2/h$, the conductance increases monotonically with increasing gate bias, showing no signs of Fabry-Perot interference. In some devices, Fabry-Perot signatures are observed; however, in each of those devices, the low- V_{sg} regime also shows quantum dot signatures [11]. These signatures are consistent with the existence of a second, unintentional potential barrier along the nanowire that creates a cavity and associated interference patterns.

While systems which support Fabry-Perot interference are expected to act as quantum dots when tuned to a tunneling regime, not all 1D quantum dot systems can exhibit Fabry-Perot interference [40]. Resonant tunneling observed in LAO/STO nanowire-based quantum dots at low V_{sg} suggests that extended coherent states exist [11], but does not rule out disorder, which randomizes carrier paths in the transport regime at high V_{sg} . In contrast, observation of Fabry-Perot interference as described here demonstrates micrometer-scale elastic scattering lengths in quasi-1D LAO/STO nanowires.

The detailed nature of the observed Fabry-Perot oscillations depends not only on the physical dimensions of the cavity, but on the band structure of the material [41]. Resonant transmission through a cavity of length L is periodic in the Fermi momentum, $k_F = n\pi/L$, so that the period is inversely proportional to length; however, a quadratic relationship between k_F and Fermi energy E_F leads to a resonance period which depends on the effective mass of the energy band, and increases with energy (see Fig. S2) [24]. Bulk STO has three degenerate $3d$ conduction bands with t_{2g} orbital character, and interfacial confinement produces an approximately 50 meV upward shift of the d_{xz} and d_{yz} bands relative to the lighter d_{xy} band [42]. Additionally, the finite width of the quasi-1D nanowire can introduce a manifold of transverse subbands. When new subbands become accessible, abrupt changes in oscillation frequency are expected and observed, further obscuring a direct relationship between device length and the interference V_{sg} period.

Observation of signatures of ballistic transport in quasi-1D LAO/STO nanowires in both the normal- and paired-electron phases contrasts with behavior reported in 2D devices. However, understanding the distinctive transport in quasi-1D structures is possibly relevant for transport measurements of the 2D LAO/STO interface, where local probes have revealed the existence of narrow channel flow along ferroelastic domain boundaries [8, 9]. Additionally, one-dimensional transport offers rich physics with many theoretical [43] predictions, including charge/spin separation [21]. Long-range coherent and ballistic transport in a strongly-correlated electronic phase, along with the reconfigurable nature of this interface system, extend the ability to design novel quantum materials.

This work was supported by ARO MURI W911NF-08-

1-0317 (J.L.), AFOSR MURI FA9550-10-1-0524 (C.B.E., J.L.), FA9550-12-1-0342 (C.B.E.), and FA9550-15-1-0334 (C.B.E.), and grants from the National Science Foundation DMR-1104191 (J.L.), DMR-1124131 (C.B.E., J.L.) and DMR-1234096 (C.B.E.).

* Present Address: Department of Physics, Grand Valley State University, Allendale, MI 49401

† Corresponding Author: jlevy@pitt.edu

- [1] A. Ohtomo and H. Y. Hwang, *Nature* **427**, 423 (2004).
- [2] P. Irvin, J. P. Veazey, G. Cheng, S. Lu, C.-W. Bark, S. Ryu, C.-B. Eom, and J. Levy, *Nano Letters* **13**, 364 (2013).
- [3] A. Brinkman, M. Huijben, M. Van Zalk, J. Huijben, U. Zeitler, J. C. Maan, W. G. Van der Wiel, G. Rijnders, D. H. A. Blank, and H. Hilgenkamp, *Nature Materials* **6**, 493 (2007).
- [4] N. Reyren, S. Thiel, A. D. Caviglia, L. F. Kourkoutis, G. Hammerl, C. Richter, C. W. Schneider, T. Kopp, A. S. Ruetschi, D. Jaccard, M. Gabay, D. A. Muller, J. M. Triscone, and J. Mannhart, *Science* **317**, 1196 (2007).
- [5] M. Ben Shalom, M. Sachs, D. Rakhmievitch, A. Palevski, and Y. Dagan, *Physical Review Letters* **104**, 126802 (2010).
- [6] A. D. Caviglia, M. Gabay, S. Gariglio, N. Reyren, C. Cancellieri, and J. M. Triscone, *Physical Review Letters* **104**, 126803 (2010).
- [7] K. A. Muller and H. Burkard, *Physical Review B* **19**, 3593 (1979).
- [8] B. Kalisky, E. M. Spanton, H. Noad, J. R. Kirtley, K. C. Nowack, C. Bell, H. K. Sato, M. Hosoda, Y. Xie, Y. Hikita, C. Woltmann, G. Pfanzelt, R. Jany, C. Richter, H. Y. Hwang, J. Mannhart, and K. A. Moler, *Nature Materials* **12**, 1091 (2013).
- [9] M. Honig, J. A. Sulpizio, J. Drori, A. Joshua, E. Zeldov, and S. Ilani, *Nature Materials* **12**, 1112 (2013).
- [10] J. P. Veazey, G. Cheng, P. Irvin, C. Cen, D. F. Bogorin, F. Bi, M. Huang, C.-W. Bark, S. Ryu, K.-H. Cho, C.-B. Eom, and J. Levy, *Nanotechnology* **24**, 375201 (2013).
- [11] G. L. Cheng, M. Tomczyk, S. C. Lu, J. P. Veazey, M. C. Huang, P. Irvin, S. Ryu, H. Lee, C. B. Eom, C. S. Hellberg, and J. Levy, *Nature* **521**, 196 (2015).
- [12] D. Rakhmievitch, M. Ben Shalom, M. Eshkol, A. Tsukernik, A. Palevski, and Y. Dagan, *Physical Review B* **82**, 235119 (2010).
- [13] X. Lin, Z. Zhu, B. Fauque, and K. Behnia, *Physical Review X* **3**, 021002 (2013).
- [14] G. Cheng, J. P. Veazey, P. Irvin, C. Cen, D. F. Bogorin, F. Bi, M. Huang, S. Lu, C.-W. Bark, S. Ryu, K.-H. Cho, C.-B. Eom, and J. Levy, *Physical Review X* **3**, 011021 (2013).
- [15] A. Ron and Y. Dagan, *Physical Review Letters* **112**, 136801 (2014).
- [16] B. J. van Wees, H. van Houten, C. W. J. Beenakker, J. G. Williamson, L. P. Kouwenhoven, D. van der Marel, and C. T. Foxon, *Physical Review Letters* **60**, 848 (1988).
- [17] P. Gallagher, M. Lee, J. R. Williams, and D. Goldhaber-Gordon, *Nature Physics* **10**, 748 (2014).
- [18] A. V. Kretinin, R. Popovitz-Biro, D. Mahalu, and H. Shtrikman, *Nano Letters* **10**, 3439 (2010).

- [19] W. J. Liang, M. Bockrath, D. Bozovic, J. H. Hafner, M. Tinkham, and H. Park, *Nature* **411**, 665 (2001).
- [20] F. Miao, S. Wijeratne, Y. Zhang, U. C. Coskun, W. Bao, and C. N. Lau, *Science* **317**, 1530 (2007).
- [21] F. D. M. Haldane, *Journal of Physics C-Solid State Physics* **14**, 2585 (1981).
- [22] Y. V. Nazarov and Y. M. Blanter, *Quantum Transport: Introduction to Nanoscience* (Cambridge University Press, Cambridge, UK ; New York, 2009).
- [23] C. Cen, S. Thiel, G. Hammerl, C. W. Schneider, K. E. Andersen, C. S. Hellberg, J. Mannhart, and J. Levy, *Nature Materials* **7**, 298 (2008).
- [24] See the Supplemental Material, which includes Refs. [25-36], for details on sample growth, nanolithography, modeling of Fabry-Perot interference, background-subtraction calculations, calculations of critical current, and single barrier devices.
- [25] J. W. Park, D. F. Bogorin, C. Cen, D. A. Felker, Y. Zhang, C. T. Nelson, C. W. Bark, C. M. Folkman, X. Q. Pan, M. S. Rzchowski, J. Levy, and C. B. Eom, *Nature Communications* **1**, 94 (2010).
- [26] C. W. Bark, D. A. Felker, Y. Wang, Y. Zhang, H. W. Jang, C. M. Folkman, J. W. Park, S. H. Baek, H. Zhou, D. D. Fong, X. Q. Pan, E. Y. Tsymbal, M. S. Rzchowski, and C. B. Eom, *Proceedings of the National Academy of Sciences of the United States of America* **108**, 4720 (2011).
- [27] C. W. Bark, P. Sharma, Y. Wang, S. H. Baek, S. Lee, S. Ryu, C. M. Folkman, T. R. Paudel, A. Kumar, S. V. Kalinin, A. Sokolov, E. Y. Tsymbal, M. S. Rzchowski, A. Gruverman, and C. B. Eom, *Nano Letters* **12**, 1765 (2012).
- [28] G. L. Cheng, P. F. Siles, F. Bi, C. Cen, D. F. Bogorin, C. W. Bark, C. M. Folkman, J. W. Park, C. B. Eom, G. Medeiros-Ribeiro, and J. Levy, *Nature Nanotechnology* **6**, 343 (2011).
- [29] A. Levy, F. Bi, M. Huang, S. Lu, M. Tomczyk, G. Cheng, P. Irvin, and J. Levy, , e51886 (2014).
- [30] S. Thiel, G. Hammerl, A. Schmehl, C. W. Schneider, and J. Mannhart, *Science* **313**, 1942 (2006).
- [31] J. N. L. Connor, *Molecular Physics* **15**, 37 (1968).
- [32] A. F. Santander-Syro, O. Copie, T. Kondo, F. Fortuna, S. Pailhes, R. Weht, X. G. Qiu, F. Bertran, A. Nicolaou, A. Taleb-Ibrahimi, P. Le Fevre, G. Herranz, M. Bibes, N. Reyren, Y. Apertet, P. Lecoeur, A. Barthelemy, and M. J. Rozenberg, *Nature* **469**, 189 (2011).
- [33] G. Kirzenow, *Physical Review B* **39**, 10452 (1989).
- [34] J. P. Veazey, G. Cheng, S. Lu, M. Tomczyk, F. Bi, M. Huang, S. Ryu, C. W. Bark, K. H. Cho, C. B. Eom, P. Irvin, and J. Levy, *Europhysics Letters* **103**, 57001 (2013).
- [35] P. Jarillo-Herrero, J. A. van Dam, and L. P. Kouwenhoven, *Nature* **439**, 953 (2006).
- [36] H. I. Jorgensen, T. Novotny, K. Grove-Rasmussen, K. Flensberg, and P. E. Lindelof, *Nano Letters* **7**, 2441 (2007).
- [37] P. Phillips and D. Dalidovich, *Science* **302**, 243 (2003).
- [38] B. Deissler, M. Zaccanti, G. Roati, C. D'Errico, M. Fattori, M. Modugno, G. Modugno, and M. Inguscio, *Nature Physics* **6**, 354 (2010).
- [39] A. W. Tsen, B. Hunt, Y. D. Kim, Z. J. Yuan, S. Jia, R. J. Cava, J. Hone, P. Kim, C. R. Dean, and A. N. Pasupathy, *Nature Physics* , Advance Online Publication 07 Dec 2015 (DOI 10.1038/NPHYS3579).
- [40] M. R. Buitelaar, A. Bachtold, T. Nussbaumer, M. Iqbal, and C. Schonenberger, *Physical Review Letters* **88**, 156801 (2002).
- [41] Q. Wang, N. Carlsson, I. Maximov, P. Omling, L. Samuelson, W. Seifert, W. D. Sheng, I. Shorubalko, and H. Q. Xu, *Applied Physics Letters* **76**, 2274 (2000).
- [42] M. Salluzzo, J. C. Cezar, N. B. Brookes, V. Bisogni, G. M. De Luca, C. Richter, S. Thiel, J. Mannhart, M. Huijben, A. Brinkman, G. Rijnders, and G. Ghiringhelli, *Physical Review Letters* **102**, 166804 (2009).
- [43] T. Giamarchi, *Chemical Reviews* **104**, 5037 (2004).

Supplemental Materials for “Micrometer-scale ballistic transport of electron pairs in LaAlO₃/SrTiO₃ nanowires”

Michelle Tomczyk,^{1,2} Guanglei Cheng,^{1,2} Hyungwoo Lee,³ Shicheng Lu,^{1,2} Anil Annadi,^{1,2} Joshua P. Veazey,^{1,*} Mengchen Huang,^{1,2} Patrick Irvin,^{1,2} Sangwoo Ryu,³ Chang-Beom Eom,³ and Jeremy Levy^{1,2,†}

¹*Department of Physics and Astronomy,*

University of Pittsburgh, Pittsburgh, PA 15260, USA

²*Pittsburgh Quantum Institute, Pittsburgh, PA, 15260 USA*

³*Department of Materials Science and Engineering,*

University of Wisconsin-Madison, Madison, WI 53706, USA

(Dated: November 8, 2021)

* Present Address: Department of Physics, Grand Valley State University, Allendale, MI 49401

† Corresponding Author: jlevy@pitt.edu

I. SAMPLE GROWTH AND PREPARATION

LaAlO₃/SrTiO₃ (LAO/STO) samples are grown by pulsed laser deposition (PLD) [S1–S3]. The STO substrate is TiO₂ terminated by etching in buffered HF for 60 seconds, and annealed at 1000°C for 6 hours to achieve an atomically smooth surface. A thin (3.4 unit cell) LAO film is subsequently grown on top of STO by PLD at a temperature of 550°C and 1×10^{-3} mbar oxygen pressure, and gradually cooled to room temperature. Electrical contact to the LAO/STO interface is made by Ar⁺ etching (25 nm) followed by sputter deposition of Ti/Au (5 nm/20 nm). Additional details are described in Ref. [S4, S5].

II. C-AFM NANOLITHOGRAPHY AND BARRIER CREATION

For LAO/STO samples grown with an LAO thickness just below the critical thickness of 4 u.c. at which the two-dimensional conducting layer appears, the interface is insulating and easily tunable by either back gate or top gate through the metal-insulator transition (MIT) [S6]. A conductive AFM (c-AFM) tip can be used as a top gate to locally induce the MIT at the interface by applying a positive voltage to the surface. Moving the positively-biased ($V \sim +10$ V) tip across the surface creates conducting structures less than 10 nm wide [S7] at the interface. These nanowires can be erased and the interface returned to an insulating state by moving a negatively biased ($V \sim -10$ V) c-AFM tip across the surface of the LAO. When a very small negative voltage (-0.05 V $< V_{tip}$ < -0.5 V) is applied to the tip, and the tip is moved perpendicularly across an existing nanowire, a nanoscale potential barrier is created in the wire. The size of the barrier is characterized by monitoring the change in resistance during the cutting process at room temperature. The cavity lengths L between the barriers ranged from 250 nm to 4 μ m. The distance from each barrier to the nearest voltage lead was held constant for all devices at 750 nm. The total distance between voltage leads (leads 3 and 4, Fig. 1a in the main text) was therefore $L + 1.5$ μ m. The 4-terminal voltage (leads 2 and 3, Fig. 1a in the main text) of a segment of nanowire equal in length to the total $L + 1.5$ μ m, but without manufactured barriers, was also measured as a control, as parameters such as V_{sg} and B were varied. The side gate was created with the same c-AFM lithography as the device, running parallel to the main current-carrying channel, about 1 μ m away. Additional details are described in Ref. [S8].

Device Name	Cavity Length L (μm)	Back gate (V)	Magnetic field in Fig. S1 (T)
A	0.25	-1	3.0
B	1.0	0	4.0
C	4.0	-3	7.0
D	1.0	-2	7.0
E	1.0	0	1.0
F	0.5	-0.7	6.0

TABLE S1. Device Parameters. Summary of cavity length L between the manufactured barriers, backgate voltage applied during measurements, and the applied magnetic field for the data in Fig. S1, for Devices A-F.

III. REPRESENTATIVE dI/dV OF SIX DEVICES

The side gate tunes both the Fermi level in the cavity and the transparency of the barriers. At very negative side gates, the nanowire cavity is very weakly coupled to the leads, resulting in diamond-shaped regions of conductance blockade (Fig. S1). This is indicative that the device is behaving as a quantum dot, with resonant tunneling only when the chemical potential of the leads aligns with an energy level on the dot. At more positive gate voltages, the barriers become more transparent. When the Fermi level in the cavity rises above the potential barriers, the device becomes conducting and the barriers act as the primary scattering centers. Long coherence and scattering lengths in the nanowires enable Fabry-Perot interference effects. Sometimes a range of V_{sg} between the blocked transport and interference oscillations exhibits a crossover regime, in which oscillations are occasionally interrupted by weak blockade, or vice versa. The full, normal-state tunability of the differential conductance (dI/dV) of Devices A, B and C in the main text, along with three other devices, is seen in Fig. S1. Interference oscillations in dI/dV appear in the conducting state of all devices, with cavity lengths ranging up to 4 microns. The device parameters are given in Table S1.

Fabry-Perot interference is expected to appear as periodic dips in a high conductance regime [S9], where the cavity is strongly coupled to the leads. The preeminence of dips, rather than peaks, has been explained by inter-mode coupling at the scattering centers [S9].

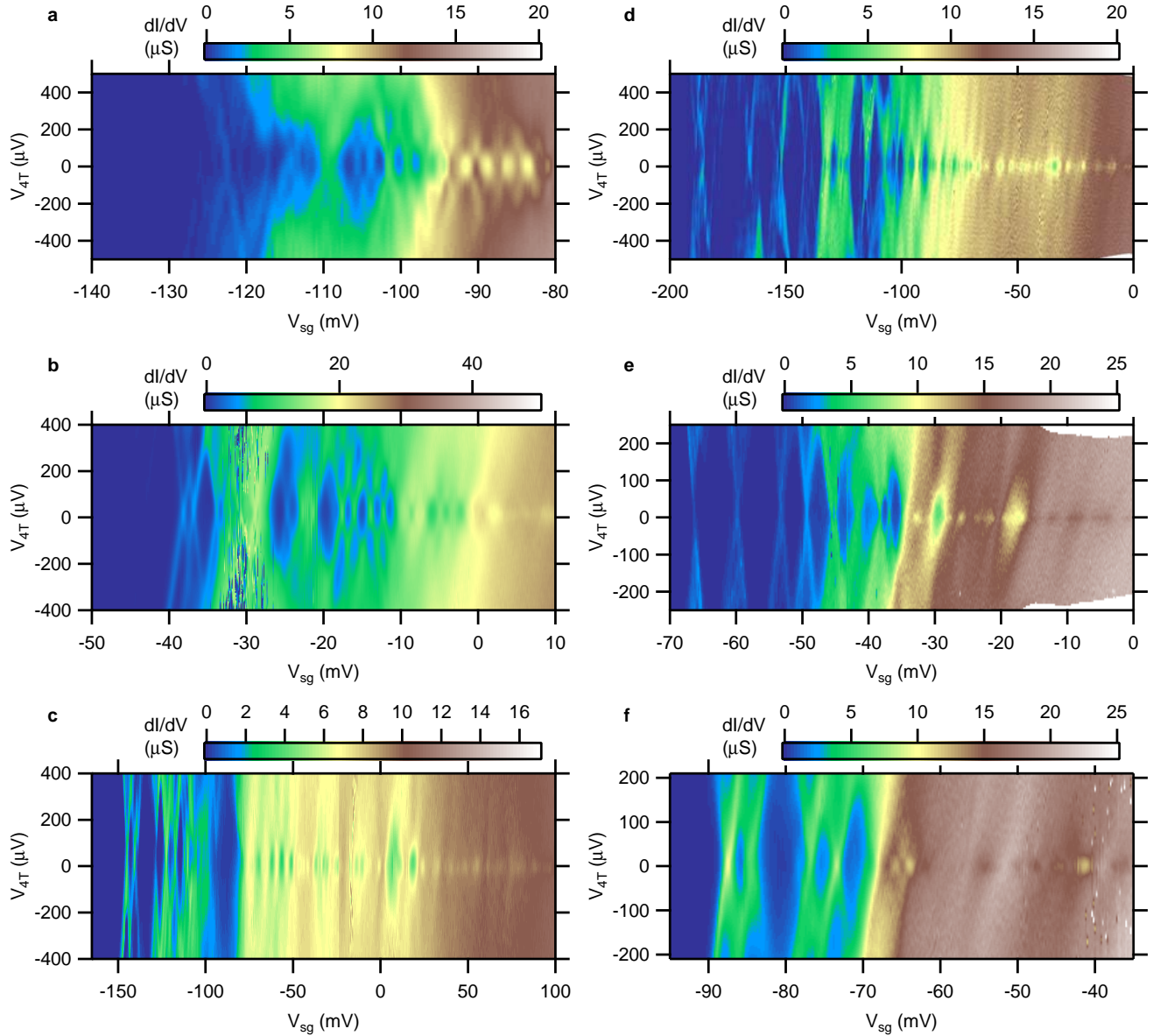


FIG. S1. Fabry Perot interference in many devices. a-f, Extended dI/dV of the cavity for Devices A-F, respectively, at $T=50$ mK. At low V_{sg} , the cavity is in the blockade regime and diamonds are present. At higher V_{sg} , the devices become conducting and Fabry-Perot oscillations are observed.

The participation of multiple subbands within the cavity increases the likelihood of inter-mode scattering, which can lead to suppression of coherence signatures. At finite bias, a range of available momenta could also suppress coherence signatures. This is likely why full checkerboard patterns only appear in small subsets of gate voltage in most devices, despite all cavity devices exhibiting zero-bias conductance oscillations.

IV. MODELING OF FABRY-PEROT INTERFERENCE

Both the geometry of the device and the band structure of the material contribute to the interference signatures in a Fabry-Perot cavity [S10, S11]. For materials with a single band, resonant transmission through a cavity of length L is periodic in the Fermi momentum, $k_F = n\pi/L$. While a linear dependence of Fermi energy E_F on momentum leads to a constant V_{sg} resonance period, a quadratic energy dispersion leads to a V_{sg} period which depends on the effective masses of the various bands, and increases with energy [S10] (1-band model in Fig. S2 a,b). Bulk STO has three degenerate $3d$ conduction bands with t_{2g} orbital character. Interfacial confinement produces a ~ 50 meV upward shift of the d_{xz}/d_{yz} bands relative to the d_{xy} band [S12], while lateral confinement in quasi-1D nanowires is expected to create a manifold of transverse subbands. Fig. S2 b shows an expected interference pattern for a nanowire with three distinct subbands.

Total conductance is calculated from the Landauer formula

$$G = \frac{e^2}{h} \sum_i T_i \quad (\text{S1})$$

where T_i are the transmission of each energy band i . In this analysis, each band is assumed to contribute e^2/h , not $2e^2/h$, because the simulation is being compared with data taken in large magnetic fields which drive the LAO/STO interface system normal and break electron pairs [S8], so that energy bands are not assumed to be spin degenerate. Transmission in a quasi-classical approximation [S11] is given by

$$\begin{aligned} T_i &= \frac{1}{P^2 + Q^2 + PQ \cos 2k_i L}; \\ P(\epsilon_L, \epsilon_R) &= \sqrt{(1 + e^{-2\pi\epsilon_L})(1 + e^{-2\pi\epsilon_R})}; \\ Q(\epsilon_L, \epsilon_R) &= e^{-\pi(\epsilon_L + \epsilon_R)}; \end{aligned} \quad (\text{S2})$$

where $\epsilon_{L,R} = (E_F - V_b)/\hbar\omega$ give the Fermi energy E_F normalized by the barrier height V_b and width ω . At each E_F , the momentum k_i for each band i with band bottom E_i below E_F was calculated for a parabolic dispersion

$$k_i = \frac{\sqrt{2m_{eff}(E_F - E_i)}}{\hbar} \quad (\text{S3})$$

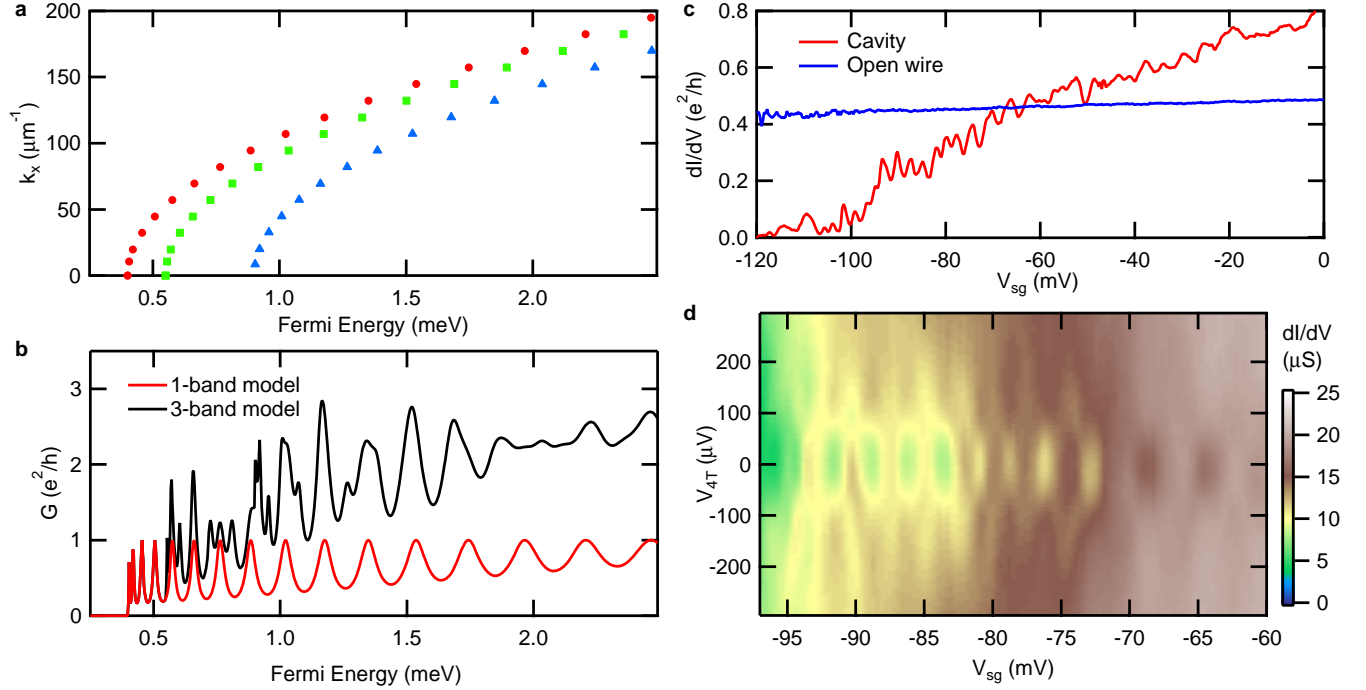


FIG. S2. Semi-classical transmission model. a, Resonant states periodic in momentum are depicted by symbols for parabolic dispersion of three bands. b, Conductance oscillations due to the lowest energy band in (a) (red) and conductance oscillations due to coherent transport of all three bands depicted in (a) (black). c, Zero-bias ($V_{4T} = 0$) differential conductance (dI/dV) of Device A ($L = 0.25 \mu\text{m}$, $B = 3 \text{ T}$) for both the cavity and the open wire. Cavity conductance features quasi-periodic oscillations that qualitatively resemble a multimode transmission model. d, dI/dV versus V_{4T} and V_{sg} for Device A show a smoothly-changing period over a subset of V_{sg} .

The three-band model in Fig. S2 uses an effective mass [S13] $m_{eff} = 0.7m_e$ for all bands, $E_1 = 300 \mu\text{eV}$, $E_2 = 550 \mu\text{eV}$ and $E_3 = 900 \mu\text{eV}$, barrier height $V_b = 100 \mu\text{eV}$, barrier width $\omega = 1 \times 10^{13} \text{ s}^{-1}$, and length of the cavity $L = 250 \text{ nm}$. The momentum states which give a maximum in T_i are shown in Fig. S2 a for the energy dispersion in Eq. (S3). For the lowest band depicted (red circles), the conductance in units of e^2/h is calculated according to Eqs. (S1-S2). Since Fig. S2 a-b share an axis, it is easy to see that each resonant state in the dispersion of the lowest (red) band in Fig. S2 a corresponds to a peak in conductance in the red curve in Fig. S2 b. The resonant states occur periodically in k_i , and therefore the spacing between resonances increases as a function of E_F . Finally, the conductance for all three bands was calculated according to Eqs. (S1-S2) (Fig. S2 b, black). In this case, beating between the

resonances occurs, resulting in what appear to be random fluctuations in conductance. Zero-bias dI/dV linecuts in the normal, unpaired state (Fig. S2 c) clearly show the qualitative similarity between the multiband model and the conductance oscillations observed in cavity devices, contrasted with the lack of such features in the open wires with no barriers. A plot of dI/dV extended to finite bias shows a slowly-increasing period between resonances, as expected, for a small range of V_{sg} (Fig. S2 d).

V. BACKGROUND SUBTRACTION

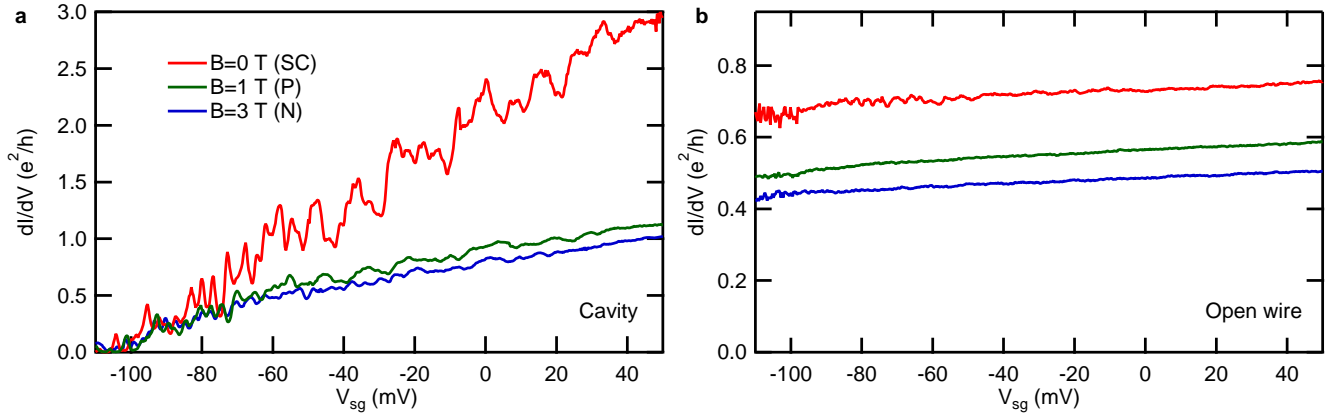


FIG. S3. Differential conductance. a-b, Zero-bias differential conductance (dI/dV) of the cavity (between voltage leads 3 and 4 in Fig. 1a in the main text) and the open wire (between leads 2 and 3) in the superconducting (red), paired (green) and normal (blue) phases of Device A.

The original zero-bias dI/dV linecuts from which the panels in Fig. 1(b) in the main text were derived are shown in Fig. S3 for both the cavity (a) and the open wire (b). A high-order polynomial fit to a V_{sg} subset from -105 to -48 mV was performed and the resulting slowly-varying background is overlaid with the original data in Fig. S4 for both the cavity and open wire in the superconducting (a), paired (b) and normal (c) phases. The root-mean-square amplitude of the fluctuations in the open wire are suppressed by over 90% compared to the cavity. Interestingly, the background conductance of the normal-state cavity reveals step-like features superimposed beneath the oscillations, reminiscent of interference oscillations originally predicted in ballistic devices with quantized conductance [S14]. While these steps are clearly much less than e^2/h , this suggests that perhaps, with refinement of

these experiments, quantized conductance is possible to achieve in these ballistic LAO/STO nanowires.

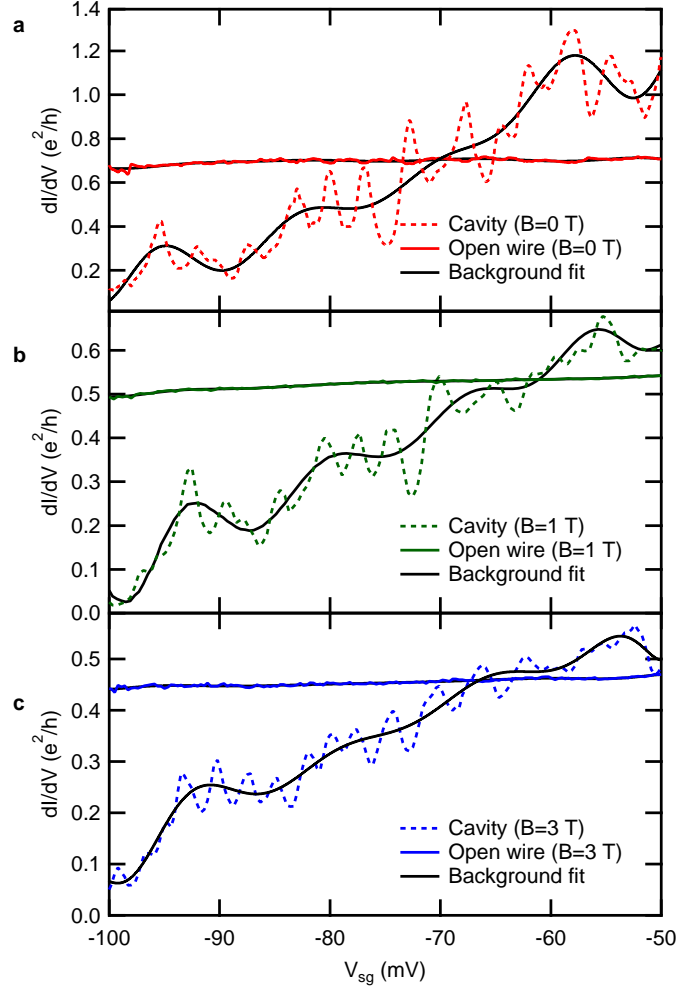


FIG. S4. Background subtraction. a-c, dI/dV of the cavity (dash) and open wire (solid color) for Device A at $B = 0$ T (a), $B = 1$ T (b) and $B = 3$ T (c). Data shown here is the subset $-100 \text{ mV} < V_{sg} < -50 \text{ mV}$ of the corresponding red, green and blue curves in Fig. S3. A slowly-varying background is overlaid on each curve (solid black). The result ΔG (Fig. 1(b) in the main text) of subtracting the slowly-varying background from dI/dV reveals Fabry-Perot interference in the cavity.

VI. SUPERCONDUCTING PHASE AND CALCULATION OF CRITICAL CURRENT

In the regime $|B| < B_c$, the device is superconducting and the conductance is significantly enhanced (Fig. S3, red) compared to the non-superconducting paired phase (green) and the normal phase (blue). While a zero-resistance superconducting state is usually not achieved in nanowires (insets of Fig. S5), likely due to the increased susceptibility of low-dimensional superconductors to thermally-activated phase slips and other effects [S15], the nanowire cavity shows a strong enhancement of conductance oscillations in the superconducting regime (Fig 1b). These features are associated with a modulation of the critical current I_c (Fig. S5), similar to supercurrent transistors [S16]. While such strong I_c modulation does not occur in the open wire, a slight anti-correlation is observed between the I_c of the cavity and open wires (e.g. $80 \text{ mV} < V_{sg} < 70 \text{ mV}$).

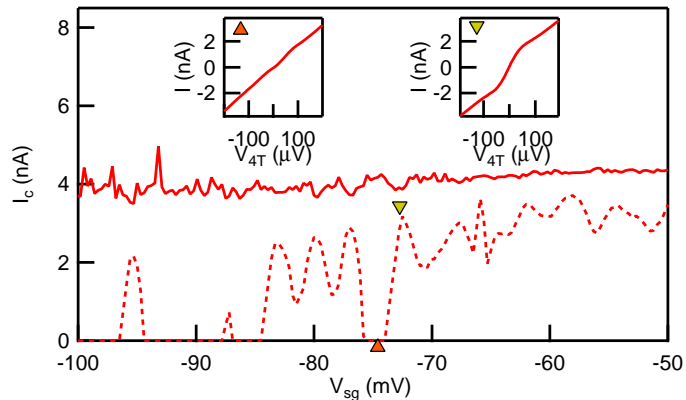


FIG. S5. Critical Current Modulations. In the superconducting state, critical current I_c of the cavity can be greatly modulated with V_{sg} , while I_c of the open wire is mostly constant. Insets show $I - V$ data resulting in low (triangle) and high (inverted triangle) I_c , which also correspond to low and high conductance oscillations.

To calculate the critical current for the cavity data, a resistive and capacitively shunted junction (RCSJ) model was used based on Ref. [S17], which models a quantum dot between two superconducting leads. The discrete energy levels due to confinement in the dot also give rise to resonant transmission in the Fabry-Perot regime. Starting with an overdamped RCSJ model with a sinusoidal current-phase relation, Ref. [S17] includes current due to Andreev

reflections and finds a current-voltage ($I - V_{sd}$) relation

$$I(V_{sd}) = I_c \operatorname{Im} \left[\frac{I_{1-i\eta(V_{sd})}(I_c \hbar / 2e k_B T)}{I_{-i\eta(V_{sd})}(I_c \hbar / 2e k_B T)} \right] + \frac{V_J(V_{sd})}{R_J};$$

$$V_J(V_{sd}) = V_{sd} - R I(V_{sd});$$

$$\eta(V_{sd}) = \hbar V_{sd} / 2e R k_B T;$$
(S4)

where $I_\alpha(x)$ is the modified Bessel function. The lead resistance R , the resistance carrying the Andreev current R_J , and the critical current I_c are the free parameters, for $T = 50$ mK. R_J is assumed to be larger than R , and this is satisfied by the fits. Examples of fits to the data which result in I_c versus V_{sg} for the cavity in Fig. S5 are shown in Fig. S6.

The RCSJ model is not appropriate for the open wire, however, because there should be no Andreev reflections, and therefore we expect $R_J < R$. Indeed, fitting the open wire $I - V_{sd}$ curves to Eq. (S4) results in $R_J < R$, invalidating the fit. Instead, we use a simpler definition. I_c for the open wire is defined as the location of the resistance peaks in the dV/dI versus I curve.

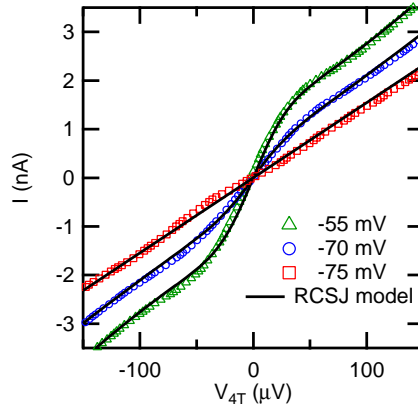


FIG. S6. Fitting data to RCSJ model. Typical current I versus voltage V_{4T} curves for the cavity in Device A at $B = 0$ T, at three V_{sg} values in the range shown in Fig. S5. Black lines are fits calculated through the RCSJ model in Eq. (S4).

VII. SINGLE-BARRIER DEVICES

Twelve devices were made with a single barrier, rather than the two barriers which define a cavity. The four-terminal leads were between 0.5-1.5 μm from the barrier, for a

total wire length of 1-3 μm between the leads for the dozen devices. Half of the devices show no blockade or Fabry-Perot, like Device G in Fig. S7. Compared to a cavity device, such as Fig. S2 c, Device G clearly has no quasi-periodic oscillations like those observed in Devices A-F (Fig. S1), even at zero-bias. The only non-linear behavior occurs as the device is pinched off by a low side gate. The other half of the single barrier devices exhibit both blockade behavior and Fabry-Perot interference, suggesting that an unintentional second barrier exists, forming a cavity. These potential barriers may contribute additional features in some of the devices with two engineered barriers. However, the disorder is not strong enough to cause blockade or Fabry-Perot signatures in open nanowires with no intentionally manufactured barriers, further supporting the claim of a long elastic scattering length.

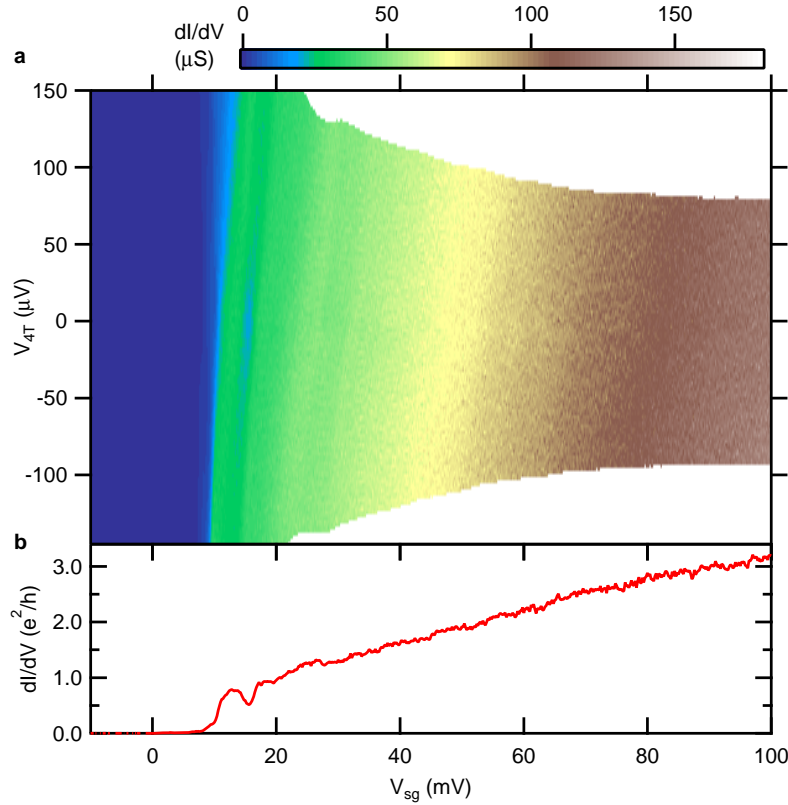


FIG. S7. Single barrier device. a, dI/dV versus V_{4T} and V_{sg} for Device G at $B = 3$ T. b, dI/dV linecut at zero-bias ($V_{4T} = 0$). No Fabry Perot conductance oscillations are observed.

-
- [S1] J. W. Park, D. F. Bogorin, C. Cen, D. A. Felker, Y. Zhang, C. T. Nelson, C. W. Bark, C. M. Folkman, X. Q. Pan, M. S. Rzchowski, J. Levy, and C. B. Eom, *Nature Communications* **1**, 94 (2010).
- [S2] C. W. Bark, D. A. Felker, Y. Wang, Y. Zhang, H. W. Jang, C. M. Folkman, J. W. Park, S. H. Baek, H. Zhou, D. D. Fong, X. Q. Pan, E. Y. Tsymbal, M. S. Rzchowski, and C. B. Eom, *Proceedings of the National Academy of Sciences of the United States of America* **108**, 4720 (2011).
- [S3] C. W. Bark, P. Sharma, Y. Wang, S. H. Baek, S. Lee, S. Ryu, C. M. Folkman, T. R. Paudel, A. Kumar, S. V. Kalinin, A. Sokolov, E. Y. Tsymbal, M. S. Rzchowski, A. Gruverman, and C. B. Eom, *Nano Letters* **12**, 1765 (2012).
- [S4] G. L. Cheng, P. F. Siles, F. Bi, C. Cen, D. F. Bogorin, C. W. Bark, C. M. Folkman, J. W. Park, C. B. Eom, G. Medeiros-Ribeiro, and J. Levy, *Nature Nanotechnology* **6**, 343 (2011).
- [S5] A. Levy, F. Bi, M. Huang, S. Lu, M. Tomczyk, G. Cheng, P. Irvin, and J. Levy, , e51886 (2014).
- [S6] S. Thiel, G. Hammerl, A. Schmehl, C. W. Schneider, and J. Mannhart, *Science* **313**, 1942 (2006).
- [S7] C. Cen, S. Thiel, G. Hammerl, C. W. Schneider, K. E. Andersen, C. S. Hellberg, J. Mannhart, and J. Levy, *Nature Materials* **7**, 298 (2008).
- [S8] G. L. Cheng, M. Tomczyk, S. C. Lu, J. P. Veazey, M. C. Huang, P. Irvin, S. Ryu, H. Lee, C. B. Eom, C. S. Hellberg, and J. Levy, *Nature* **521**, 196 (2015).
- [S9] W. J. Liang, M. Bockrath, D. Bozovic, J. H. Hafner, M. Tinkham, and H. Park, *Nature* **411**, 665 (2001).
- [S10] Q. Wang, N. Carlsson, I. Maximov, P. Omling, L. Samuelson, W. Seifert, W. D. Sheng, I. Shorubalko, and H. Q. Xu, *Applied Physics Letters* **76**, 2274 (2000).
- [S11] J. N. L. Connor, *Molecular Physics* **15**, 37 (1968).
- [S12] M. Salluzzo, J. C. Cezar, N. B. Brookes, V. Bisogni, G. M. De Luca, C. Richter, S. Thiel, J. Mannhart, M. Huijben, A. Brinkman, G. Rijnders, and G. Ghiringhelli, *Physical Review Letters* **102**, 166804 (2009).

- [S13] A. F. Santander-Syro, O. Copie, T. Kondo, F. Fortuna, S. Pailhes, R. Weht, X. G. Qiu, F. Bertran, A. Nicolaou, A. Taleb-Ibrahimi, P. Le Fevre, G. Herranz, M. Bibes, N. Reyren, Y. Apertet, P. Lecoeur, A. Barthelemy, and M. J. Rozenberg, *Nature* **469**, 189 (2011).
- [S14] G. Kirczenow, *Physical Review B* **39**, 10452 (1989).
- [S15] J. P. Veazey, G. Cheng, S. Lu, M. Tomczyk, F. Bi, M. Huang, S. Ryu, C. W. Bark, K. H. Cho, C. B. Eom, P. Irvin, and J. Levy, *Europhysics Letters* **103**, 57001 (2013).
- [S16] P. Jarillo-Herrero, J. A. van Dam, and L. P. Kouwenhoven, *Nature* **439**, 953 (2006).
- [S17] H. I. Jorgensen, T. Novotny, K. Grove-Rasmussen, K. Flensberg, and P. E. Lindelof, *Nano Letters* **7**, 2441 (2007).